

Many-body dynamical localization and thermalization

Christine Khripkov^{1,2}, Amichay Vardi¹, Doron Cohen²

¹*Department of Chemistry, Ben-Gurion University of the Negev, Beer-Sheva 84105, Israel*

²*Department of Physics, Ben-Gurion University of the Negev, Beer-Sheva 84105, Israel*

We demonstrate dynamical localization in a generic setup of two weakly-coupled chaotic subsystems. The minimal subsystem of experimental interest is a 3-mode Bose-Hubbard trimer. We clarify the procedure for identification of a mobility edge in the chaotic sea, beyond which dynamical localization suppresses ergodization, and hence arrests the thermalization process.

I. INTRODUCTION

The study of *dynamical* localization in low dimensional chaotic system was pioneered in the publication “Chaos, Quantum Recurrences, and Anderson Localization” by Shmuel Fishman, D.R. Grempel and R.E. Prange [1], which had been motivated by the puzzling numerical observations of Casati, Chirikov, Izrailev and Ford [2]. For an extended period, most research efforts focused on the quantum kicked rotor system, regarded as the quantized version of the “Standard map” (see [3] and references within). This system has one degree of freedom (dof), and driving effectively adds an extra half dof.

In a recent manuscript [4] we have taken this type of localization, that is not related to *disorder* and does not necessitate an infinite-dof chain, to the realm of many-body quantum chaos. Our study involved a minimal Bose-Hubbard model for many-body thermalization, namely, a trimer-monomer system that has 2+1 dof. We have demonstrated that *dynamical* localization manifests itself in this system, and developed a theory for it, by combining the breaktime phenomenology of Chirikov and followers [5–8] with the phase space exploration phenomenology of Heller [9].

In this work, we establish that dynamical localization is present in the more generic case of trimer-trimer thermalization. The main conceptual difference from the trimer-monomer model is that here both subsystems are chaotic. The implication is that dynamical localization is relevant also for larger disordered arrays, because they can be viewed as chains of weakly interacting subsystems, some of which (or all) are chaotic. It should be reemphasized that unlike the disorder-induced many-body localization (MBL) [10, 11], the cause of dynamical localization in this work, is interaction-induced chaos on the microscopic scale, and the thermodynamic limit is not an issue.

Outline.— In Section II we introduce the model Hamiltonian, characterize the trimer as a subsystem, and define the required representation for the discussion of the thermalization process. Numerical demonstration of dynamical localization is provided in Section III. The ergodicity measure whose objective is to identify the mobility edges of the chaotic sea, is defined in Section IV and used for the analysis of classical localization in Section V and of quantum localization in Section VI. Finally, in section VII we emphasize the non-triviality of the observed

dynamical localization, as opposed to perturbative localization on the one hand, and semiclassical non-ergodicity on the other.

II. THE MODEL

Our building blocks are a pair of Bose-Hubbard trimers, labeled by $\alpha = L, R$. Each trimer is described by the Hamiltonian

$$\mathcal{H}_\alpha = \frac{U}{2} \sum_{j=1}^3 \hat{n}_{\alpha j}^2 - \frac{K}{2} \sum_{j=1,3} \left(\hat{a}_{\alpha j}^\dagger \hat{a}_{\alpha 2} + \text{H.c.} \right). \quad (1)$$

The operators $\hat{a}_{\alpha j}^\dagger$ and $\hat{a}_{\alpha j}$, respectively, create or annihilate a particle on site αj , while $\hat{n}_{\alpha j} = \hat{a}_{\alpha j}^\dagger \hat{a}_{\alpha j}$ counts particles in this site. The parameter K is the tunneling strength between neighboring sites, while U describes interaction between two particles. In the absence of inter-trimer coupling (and for our particular choice of coupling, see below), the populations $N_\alpha = \sum_j \hat{n}_{\alpha j}$ are separately conserved. The total number of particles is $N = N_L + N_R$.

Instead of using the local site basis, it is possible to define three *orbitals* (superpositions of site states) that diagonalize the noninteracting Hamiltonian (see Appendix A). In particular we define a ‘dark’ orbital that is associated with the operator $\hat{a}_{\text{dark}} = (1/\sqrt{2})(\hat{a}_1 - \hat{a}_3)$.

The spectrum of an isolated trimer (say, $\alpha=R$) is illustrated in Fig. 1a for $u = 6$. Each point represents an eigenstate $|E_R\rangle$ of the Hamiltonian \mathcal{H}_R , positioned horizontally according to its eigenenergy $\varepsilon \equiv \langle \mathcal{H}_R \rangle / N_R$, and vertically according to the expectation value of the dark orbital occupation $I_{\text{dark}} \equiv \langle \hat{n}_{\text{dark}} \rangle / N_R$. The points are color-coded by the one-particle purity of the eigenstates: high purity implies a coherent state where all particles occupy a single orbital (see Appendix A).

In the classical limit, the Hamiltonian of Eq. (1) describes the motion of coupled non-linear oscillators. We can derive the classical equations of motion for the occupations and propagate them, to obtain classical power spectrum of the site occupations, shown in Fig. 1b,c. Within the central energy region the classical motion has a wide frequency content, which is the hallmark of chaos (see Appendix B,C). Fig. 1d displays the r -measure of level spacing statistics (see Appendix B). We witness, as

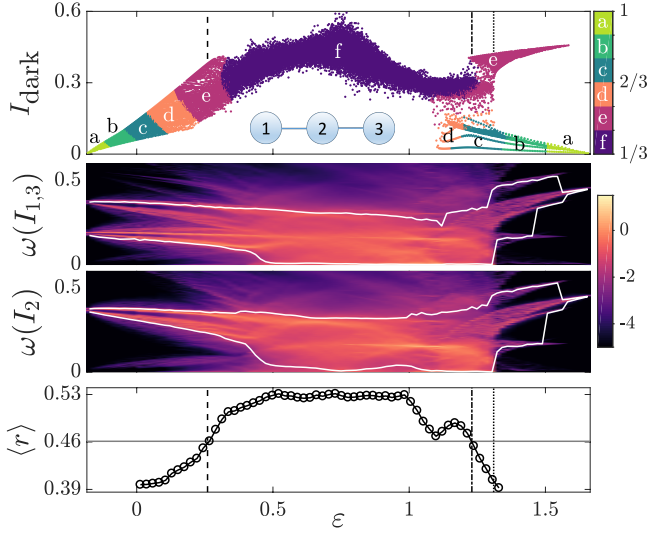


FIG. 1. (Color online) The spectrum of an isolated trimer. Top panel: Each point represents an eigenstate $|\varepsilon\rangle$ for $N_\alpha = 350$ particles and $u = 6$, positioned according to its energy ε , and the expectation value I of the dark orbital occupation. The points are color-coded by purity. Inset: the isolated trimer. Central panels: The power spectra of $I_{1,2,3}(t)$, color-coded using a \log_{10} scale. Each column is the average spectrum for a different value of ε . The white boundaries enclose 95% of the total power. Lowest panel: the locally-averaged level spacing correlation function for $N_\alpha = 450$. The chaotic range is defined as the energies for which $\langle r \rangle$ lies above the horizontal line that distinguishes Wigner from Poisson statistics [$(\langle r \rangle_{\text{Poisson}} + \langle r \rangle_{\text{Wigner}})/2 = 0.461$]. Vertical lines indicate the lower and upper chaos borders (dashed and dot-dashed) and the self-trapping threshold (dotted).

expected, that classical chaos is reflected in the quantum spectrum within the energy range $0.26 < \varepsilon < 1.23$. This has been further verified by direct classical phase space analysis as in [12].

Considering the two trimers together, yet without interaction, we obtain the energy landscape illustrated in Fig. 2. Each point represents an eigenstate $|E, x\rangle$ of $\mathcal{H}_R + \mathcal{H}_L$, positioned according to

$$\begin{aligned} E &= \frac{1}{2}(\varepsilon_R + \varepsilon_L), \\ x &= (\varepsilon_R - \varepsilon_L). \end{aligned} \quad (2)$$

Given the single trimer density of states $g(\varepsilon)$, the joint density of states with respect to x , within the energy shell $[E_0, E_0 + dE]$, determines the ergodic distribution. Namely,

$$P_{\text{erg}}(x) \propto g(E_0 + x/2) g(E_0 - x/2). \quad (3)$$

This is the distribution of x for a microcanonical ensemble in phase space. Considering the very long time propagation of a localized cloud, for weak inter-trimer coupling this distribution would be obtained if the dynamics were strictly ergodic within the energy shell, regardless of the details of the initial preparation.

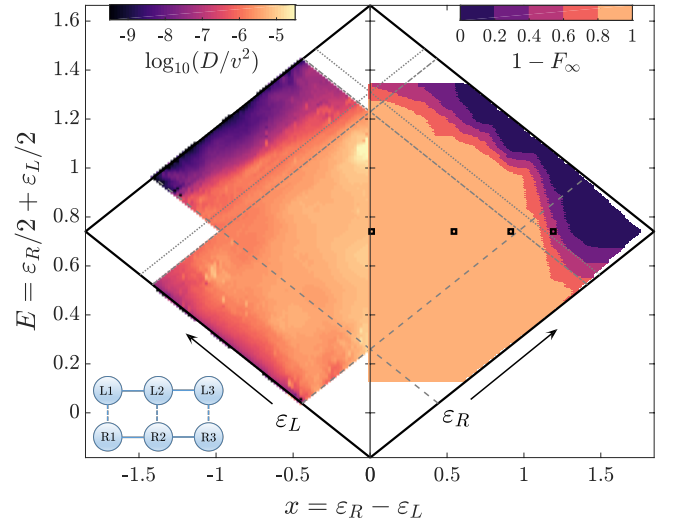


FIG. 2. (Color online) The spectrum of the non-interacting ($v = 0$) double-trimer with $u = 6$. Each direct product eigenstate of $\mathcal{H}_L + \mathcal{H}_R$ is represented by a point in the (E, x) plane. For a large N these points form a dense lattice within the classically allowed range (marked by the black boundary). The diagonal lines indicate the lower and upper chaos borders (dashed and dot-dashed) and the self-trapping threshold (dotted). Markers indicate the simulations of Fig. 3. In the left half of the spectrum, color indicates the value of the scaled diffusion coefficient D . In the right half the color reflects the ergodicity measure F_∞ , evaluated for classical simulations at $tv^2 = 450$. High values of F_∞ correspond to ergodicity; low values imply localization, correlating with negligibly small D . Inset: the configuration of the double trimer system; adjacent sites within a trimer are strongly coupled (solid lines); sites that belong to different trimers are weakly coupled (dashed lines).

In order to simulate a thermalization process, the two trimer subsystems are weakly coupled. For this purpose we employ the nearest-neighbour interaction of particles that occupy the same j -location,

$$\mathcal{H} = \mathcal{H}_L + \mathcal{H}_R + \mathcal{H}_c, \quad (4)$$

$$\mathcal{H}_c = \frac{V}{2} \sum_{j=1}^3 \hat{n}_{Lj} \hat{n}_{Rj}, \quad (5)$$

with V denoting the nearest-neighbour interaction strength. This extended Bose-Hubbard model [13, 14] can be realized using the long-range dipole-dipole interaction between lattice-BECs of particles with electric or magnetic dipole moments [15, 16]. Within each trimer the nearest-neighbor interaction would be small with respect to the intra-trimer hopping frequency, and could thus be neglected. However, nearest-neighbor interaction can dominate the coupling of the two trimers, provided the energy barrier between them is sufficiently high to preclude inter-trimer hopping. This type of coupling allows energy flow between the trimer subsystems (x is not a constant of motion), but excludes particle exchange.

Practically, it allows for a full many-body numerical solution up to $N \sim 50$, which would be impossible had we allowed inter-trimer tunneling. Note that in our previous work on the thermalization of a trimer-monomer system [4], particle exchange was allowed and x was the occupation difference. We shall see that the physics of dynamical localization is robust, and does not depend on such details.

The dimensionless parameters of the model are $u \equiv UN/K$ (intra-trimer nonlinearity) and $v \equiv VN/K$ (inter-trimer coupling). The units can be chosen such that $K = 1$. In what follows, we refer to the exact many-body evolution under the Hamiltonian of Eq. (4) as the *quantum dynamics*, whereas its large N classical limit is obtained by replacing the field operators by c -numbers. We use the term *semiclassical propagation* to denote the classical propagation of a cloud (as in the truncated Wigner approximation). The classical amplitudes can be scaled, such that $a_{\alpha j} = \sqrt{N_\alpha I_{\alpha j}} e^{i\varphi_{\alpha j}}$, where the scaled occupations $I_{\alpha j} \in [0, 1]$ and the phases $\varphi_{\alpha j} \in [0, 2\pi)$ are canonical action-angle variables. In terms of these variables the scaled classical Hamiltonian takes the form

$$\mathcal{H}_\alpha^{\text{cl}} = \frac{u}{4} \sum_{j=1}^3 I_{\alpha j}^2 - \sum_{j=1,3} \sqrt{I_{\alpha j} I_{\alpha 2}} \cos(\varphi_{\alpha j} - \varphi_{\alpha 2}), \quad (6)$$

$$\mathcal{H}_c^{\text{cl}} = \frac{v}{8} \sum_{j=1}^3 I_{Lj} I_{Rj}. \quad (7)$$

III. SPREADING AND ERGODIZATION

The exact dynamics of the quantum many-body system is analysed via the time-dependent probability distribution

$$P_t(E, x | E_0, x_0) = |\langle E, x | e^{-i\mathcal{H}t} | E_0, x_0 \rangle|^2. \quad (8)$$

The x range is divided into bins of width dx . For a given initial state $|E_0, x_0\rangle$ we define the coarse-grained distribution

$$P_t(x) = \sum_{x < x' < x+dx} P_t(E, x' | E_0, x_0). \quad (9)$$

Finally, we average over sufficiently long time to obtain a relatively smooth saturation profile. Formally we write:

$$P_\infty(x) = \lim_{t \rightarrow \infty} \frac{1}{t} \int_0^t P_t(x) dt. \quad (10)$$

Semiclassically, we assume an initial preparation that is represented by a microcanonical cloud of points within (E_0, x_0) region that is determined by the *unperturbed* Hamiltonian of uncoupled trimers. The numerical procedure is described in Appendix C. Individual points of the cloud are propagated under the canonical equations of motion $da_{\alpha j}/dt = \partial \mathcal{H} / \partial a_{\alpha j}^*$. The equations of motion

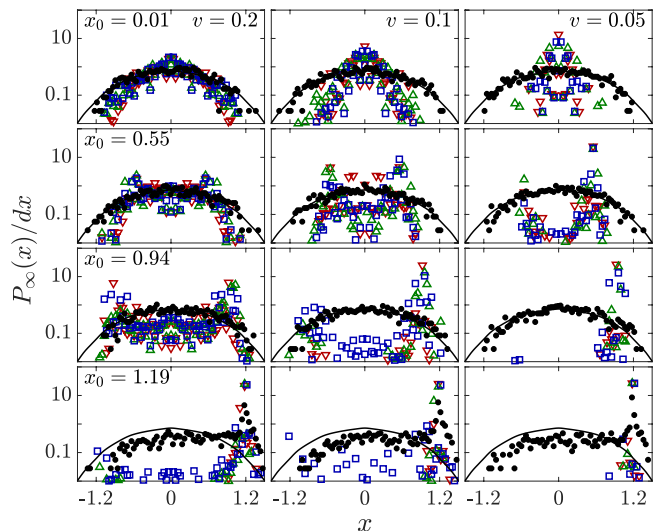


FIG. 3. (Color online) Quantum (colored markers) and classical (black markers) long-time probability distributions $P_\infty(x)$, compared with the ergodic distribution $P_{\text{erg}}(x)$ (solid black line). The quantum simulations with $N_L = N_R = 24$ are initiated in three randomly chosen unperturbed direct product states with similar values of x_0 and E_0 . The classical simulations are for a corresponding cloud of 1000 randomly selected phase space points uniformly covering the corresponding (E_0, x_0) region. The initial energy is $E_0 = 0.74 (\pm 0.02)$ for quantum simulations). The value of x_0 varies with each row, while the value of v varies with each column. The total simulation time is $tv^2 = 10^4$ (quantum) or $tv^2 = 450$ (classical). The initial conditions are marked by symbols in Fig. 2.

for the action-angle variables themselves are not well-defined since they contain terms with I_j in the denominator, yielding infinite rates whenever any $I_j \rightarrow 0$. The final distribution of points $P_t(x)$ is obtained by counting the number of points falling within each bin $(x, x+dx)$ at a time t .

Figure 3 displays the results of representative simulations. The initial energy, E_0 , is the same for all simulations, while the initial trimer energy difference, x_0 , is different for each row of panels [those initial conditions are marked in Fig. 2]. The value v is different for each column. The probability distribution $P_\infty(x)$ in the long time limit can be compared with the ergodic distribution $P_{\text{erg}}(x)$, indicated by the black line. We see that the classical simulations leads to an ergodic distribution for $x_0 = 0.01, 0.55, 0.94$ but not for $x_0 = 1.19$, irrespective of v . By contrast, the quantum simulations are sensitive to v , and either approach the ergodic distribution for a more limited range of x than their classical counterparts, or are completely non-ergodic. Our objective is to quantify this observation.

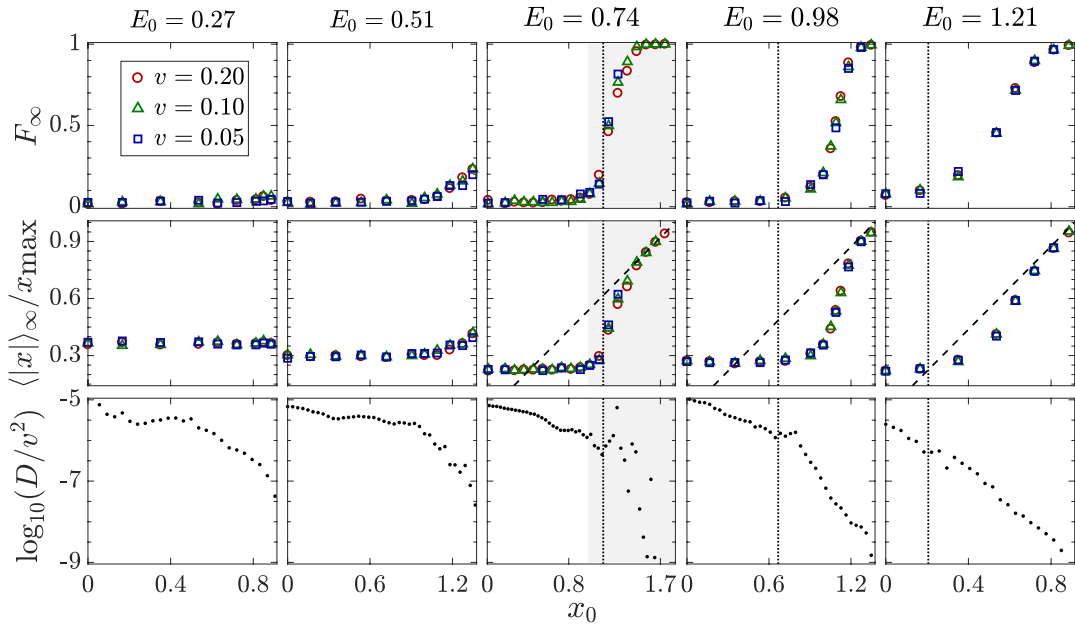


FIG. 4. (Color online) Classical ergodicity for representative simulations. Each column corresponds to the same E_0 (indicated above the column) and varying x_0 . Top panels: the ergodicity measure. Middle panels: the mean value of $|x|$, evaluated from $P_\infty(x)$, divided by the highest classically-allowed value of x for the given E . The diagonal line is $\langle |x| \rangle_\infty = x_0$. Localization is implied by $\langle |x| \rangle_\infty \sim x_0$ and low F_∞ . Lower panels: the diffusion coefficient of Eq. (13). The localization observed in the top and middle panels when one of the trimers is self-trapped correlates with very low values of D . Total simulation time is $tv^2 = 450$. Vertical lines mark the self-trapping energy. In the grey areas (central column) both trimers are quasi-integrable.

IV. THE ERGODICITY MEASURE

Attempting to quantify ergodicity, the first inclination is to define a measure that would compare $P_\infty(x)$ to $P_{\text{erg}}(x)$. We employ the Kolmogorov-Smirnov test: if $F(x)$ is the cumulative distribution function,

$$F(x) = \sum_{x' \leq x} P(x'), \quad (11)$$

then the measure of ergodicity is given by

$$F_\infty \equiv \max_x |F(x) - F_{\text{erg}}(x)|. \quad (12)$$

Two completely different distributions (i.e., having no overlap) yield $F_\infty = 1$. On the other hand, $F_\infty \rightarrow 0$ implies ergodicity. The results are presented in Fig. 4a for classical simulations with different initial conditions. Note that these results are also incorporated into Fig. 2.

In a mixed phase space system, containing both chaotic and quasi-integrable regions, the energy surface as a whole is not ergodic. It is only the connected “chaotic sea” region that can be regarded as ergodic. Furthermore, in the quantum case some peripheral regions of the sea may not be accessible, if the wavepacket has to percolate via sub-Planck corridors. We therefore would like to adopt an *intrinsic* definition of ergodicity that does not depend on our prejudice regarding the phase space structure, and does not involve comparison with $P_{\text{erg}}(x)$. Accordingly, below we use the term *ergodic region* for the

region in which there is no memory of the initial conditions. It is the region where $P_\infty(x)$ becomes independent of x_0 . By contrast, in non-ergodic regions the obtained $P_\infty(x)$ depends on x_0 , with the particular extreme case of *localization*, where $P_\infty(x)$ is peaked around the initial value $x = x_0$.

In principle, a full comparison of the distributions $P_\infty(x)$ for different x_0 is required for our memory-based intrinsic ergodicity measure. In practice, for the purpose of quantitative analysis it is more effective to consider just a single moment of the long-time distribution, and examine its sensitivity to x_0 . Due to the system’s mirror symmetry (since we set $N_R = N_L$) we choose $\langle |x| \rangle_\infty$ for this purpose. The results in the classical case are presented in Fig. 4b; they correlate well with the non-intrinsic F measure.

V. CLASSICAL LOCALIZATION

In the right half of Fig. 2 the double-trimer spectrum is colored according to the value of the ergodicity measure F_∞ . The ergodic phase space region can be identified from the (E, x) values where F_∞ is low. Outside of this region we distinguish between several classical localization mechanisms (see Appendix A).

The first possibility is quasi-integrability due to *quasi-linearity*. A single trimer is not chaotic in the linear, low energy region of its spectrum. When two such trimers are

coupled (the lower corner of Fig. 2), if v is small enough the dynamics is likely to remain quasi-integrable, and therefore thermalization would be avoided. In fact, we have to restrict all such statements, and point out that due to Arnold diffusion we can always have thermalization after an exponentially long time.

The second possibility is *self-trapping* which is localization within an isolated part of the energy surface that is surrounded by a (higher or lower energy) forbidden region. A single trimer becomes self-trapped when its energy is above a well-defined border and is therefore dominated by interaction. When two self-trapped trimers are coupled (the upper corner of Fig. 2), or when a self-trapped trimer is coupled to a quasi-linear one (the left and right corners of Fig. 2), energy exchange is suppressed due to the regular motion in each trimer.

By contrast, if a self-trapped trimer is coupled to a chaotic one, energy exchange should occur; the situation is similar to a system of harmonic oscillators under stochastic driving, or, in reverse, a system of chaotic oscillators under harmonic driving. However, in our coupled trimer system we still obtain classical localization. To understand this, consider the Fokker-Plank picture of thermalization [12]. The diffusion coefficient D for spreading in ε is given by the classical version of the Fermi-Golden-Rule:

$$D = \left(\frac{v}{8}\right)^2 \sum_{j=1}^3 \frac{1}{2} \int_{-\infty}^{\infty} \frac{d\omega}{2\pi} \tilde{S}_j(\omega; \varepsilon_L) \tilde{S}_j(\omega; \varepsilon_R) \omega^2. \quad (13)$$

This expression assumes that the two subsystems are independent and weakly coupled. In the present context $\tilde{S}_j(\omega; \varepsilon)$ is the power spectrum of the fluctuating variable $I_j(t)$ (see Appendix B). This linear-response expression implies that the dynamics for different v values should be identical when observed on a $\tilde{t} = tv^2$ scale.

The resulting value of D for selected initial conditions is shown in Fig. 4c, and for the entire spectrum in the left part of Fig. 2. As observed in Fig. 1b,c, the narrow range of frequencies associated with self-trapped motion should have only a small overlap with the wide band resulting from chaotic motion. Indeed, very low values of D are correlated with self-trapping in one of the trimers.

Summarizing, thermalization in classical context is generally expected whenever either one or both subsystems are chaotic. In our previous work on the trimer-monomer system, ergodization is obtained whenever the trimer is chaotic despite the integrability of the monomer. However, here we have encountered a situation where the expected thermalization process is suppressed due to a vanishingly small value of D .

VI. QUANTUM LOCALIZATION

We apply the same analysis as in the classical case for the quantum distributions $P_{\infty}(x)$ that are obtained from long time simulations with different initial values

x_0 . The results are presented in Fig. 5. The first striking difference compared with to the classical simulation is the strong v dependence. As v is increased the classical limit is approached, but even for large v ergodicity is not attained. Even in the central region where $x_0 \approx 0$ we observe some memory of the initial conditions.

Before further discussing this v dependence, we point out that there is a shortcut for obtaining the quantum saturation profile. Using the short notation $|X\rangle \equiv |E, x\rangle$, and expanding each state in the basis $|E_n\rangle$ of \mathcal{H} , the time dependent distribution takes the form

$$P_t(X) = \sum_{n,m} \langle X|E_n\rangle \langle E_n|X_0\rangle \langle X_0|E_m\rangle \langle E_m|r\rangle e^{i(E_m-E_n)t}.$$

Upon time averaging, for a nondegenerate spectrum, the oscillating terms cancel out and one obtains the result $P_{\infty}(X) = P_{\text{sat}}(X)$ where

$$P_{\text{sat}}(X) = \sum_n |\langle X|E_n\rangle|^2 |\langle E_n|X_0\rangle|^2. \quad (14)$$

Due to the mirror symmetry of our double trimer system, it is clear that all eigenstates have a definite parity (see Appendix D), and therefore the x -projected saturation profile satisfies $P_{\text{sat}}(-x) = P_{\text{sat}}(x)$. Contrary to this expectation, some simulations give $P_{\infty}(-x) \neq P_{\infty}(x)$ (see examples in Fig. 3). This happens due to quasi-degeneracies in the spectrum $\{E_n\}$ that are present for small v and which cannot be resolved in a finite time simulation. These quasi-degeneracies are remnants of the exact $v = 0$ degeneracy of the $|E, \pm x\rangle$ states.

We define the x -basis participation number,

$$M \equiv \left[\sum_x P(x)^2 \right]^{-1}. \quad (15)$$

Whenever the quasi-degenerate states significantly contribute to the dynamics, we are likely to observe very little spreading, meaning that $M \sim 2$ (see Fig. 6a), with $M = 2$ being the minimal value for $x_0 \neq 0$ due to the mirror symmetry. This is just a trivial *perturbative localization* taking place because the v -related couplings are small compared to the mean level spacing. In our system the density of states becomes smaller at peripheral (large $|x|$) regions, hence localization there might be of this benign type. However, looking at Fig. 6a we also see regions where M is significantly larger than unity. Classical intuition suggests that ergodization should take place within these regions. But looking on the numerical results of Fig. 5b we clearly see that in the quantum case there is a residual memory of x_0 , which is a signature of a non-trivial dynamical localization effect.

Coming back to the discussion of $P_{\infty}(x)$ vs $P_{\text{sat}}(x)$, we plot in Fig. 6b the ratio $M_{\infty}/M_{\text{sat}}$. This can be regarded as a measure for the relative contribution of quasi-degeneracies. Whenever the the initial state significantly overlaps quasi-degenerate pairs, we get $P_{\infty}(x) = 2P_{\text{sat}}(x)$ for $x > 0$ and zero otherwise (we always start with

$x_0 > 0$). Consequently the ratio M_∞/M_{sat} drops from 1 to $1/2$. This discussion clarifies our choice of $\langle |x| \rangle_\infty$ rather than $\langle x \rangle_\infty$ as a measure for the characterization of the spreading profile. Strictly, the latter will be always zero in the infinite time limit irrespective of localization, merely due to the mirror symmetry of the system.

VII. SUMMARY

Localization is commonly viewed as an interference phenomenon that leads to a breakdown of quantum-classical correspondence. Such definition is not *intrinsic*: it requires an *a priori* definition of some reference space and a measure that compares the actual quantum spreading to a different (classical) dynamics. This point of view is quite frustrating when dealing with small quantized systems, because in practice the correspondence is quite bad to begin with. We therefore prefer to view localization as lack-of-ergodicity, and to provide a measure for *intrinsic ergodicity*. We have defined ergodicity as the case of having some space within which the saturation profile becomes independent of the initial conditions. Accordingly, we could analyze *separately* the ergodicity in the classical case and in the quantum case, and then independently compare the two.

One should remember that several mechanisms can lead to *localization*. The most trivial one, as in the case of a single trimer with large u , is self-trapping. This is classical localization due to energetic stability within an isolated region of the energy surface. A more complex type of classical localization arises due to dynamical stability of quasi-linear motion. The latter case is endangered by Arnold diffusion, which, in practice, can be ignored due to unrealistic time scales.

Our aim in this work was to highlight the emergence of *quantum* dynamical localization effect in the thermalization process of weakly coupled subsystems. The term *weak coupling* is used in a classical sense; quantum mechanically, the coupling might lead to mixing of many levels. In fact, the extreme case of weak coupling in the quantum sense is not very interesting at all, because it leads to a *perturbative localization*, indicated by $M \sim 2$ participation numbers (i.e., no spreading happens). However, we do observe clear signs of quantum localization even when the coupling is not trivially small, so that M is large. We were thus able to demonstrate a quantum mechanical loss of *intrinsic ergodicity* despite having non-perturbative quantum mixing. This is the novel type of quantum dynamical localization.

Acknowledgment.— The present line of study has been inspired by discussions with Shmuel Fishman who passed away recently (2-April-2019). This research was supported by the Israel Science Foundation (Grant No.283/18).

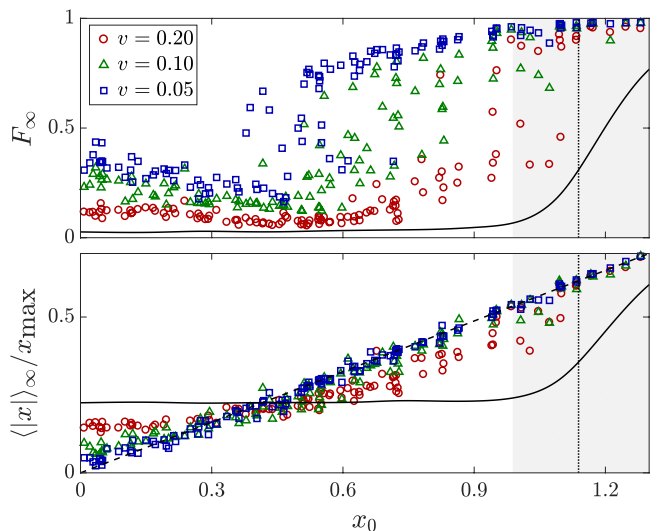


FIG. 5. (Color online) Quantum ergodicity for representative simulations. For all simulations $E_0 = 0.74$ and $N_L = N_R = 24$. Top panel: the ergodicity measure F_∞ . Bottom panel: the mean value of $|x|$, evaluated from $P_\infty(x)$, divided by the highest classically-allowed value of x for the given E . The diagonal line is $\langle |x| \rangle = x_0$. Vertical lines mark the self-trapping energy. In the grey area both trimers are quasi-integrable. Total simulation time is $tv^2 = 10^4$. The v -independent classical values (extrapolated based on Fig. 4) are indicated by the black curve. The x -range was cutoff for readability; in the discarded region $F_\infty \approx 1$ and $\langle |x| \rangle_\infty \approx x_0$.

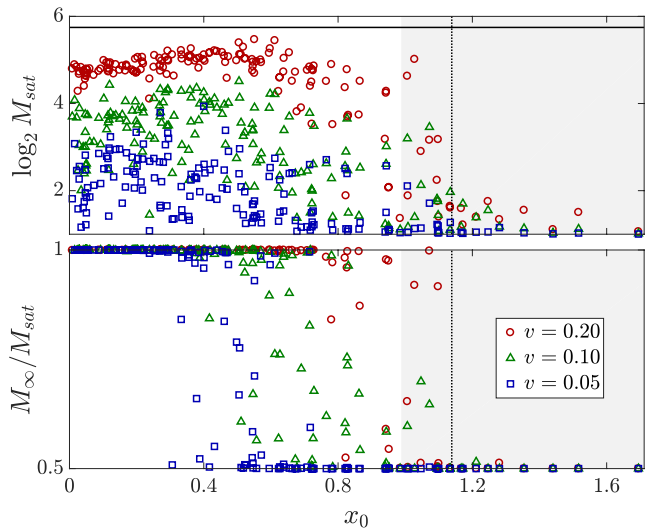


FIG. 6. (Color online) Saturation of the quantum simulation. The initial states are identical to those of Fig. 5. Top panel: the participation number of the saturation profile. The ergodic limit is indicated by the horizontal line. Lower panel: the ratio of participation numbers based on the long-time-averaged probability distribution and the saturation profile. Vertical lines mark the self-trapping energy. In the grey areas both trimers are nonchaotic.

-
- [1] S. Fishman, D. R. Grempel, and R. E. Prange, Phys. Rev. Lett. **49**, 509 (1982).
 - [2] G. Casati, B. V. Chirikov, F. M. Izrailev and J. Ford, in *Stochastic Behaviour in classical and Quantum Hamiltonian Systems*, edited by G. Casati and J. Ford, Lecture Notes in Physics, Vol. 93 (Springer, Berlin, Heidelberg, 1979), p. 334.
 - [3] B. Chirikov and D. Shepelyansky, Scholarpedia, **3**, 3550 (2008).
 - [4] C. Khripkov, A. Vardi, and D. Cohen, Phys. Rev. E **97**, 022127 (2018).
 - [5] B. V. Chirikov, Phys. Rep. **52**, 263 (1979).
 - [6] D. L. Shepelyansky, Physica D **28**, 103 (1987).
 - [7] T. Dittrich, Phys. Rep. **271**, 267 (1996).
 - [8] D. Cohen, J. Phys. A **31**, 277 (1998).
 - [9] E. J. Heller, Phys. Rev. A **35**, 1360 (1987).
 - [10] D. M. Basko, I. L. Aleiner, and B. L. Altshuler, Annals of Physics **321**, 1126 (2006).
 - [11] I. L. Aleiner, B. L. Altshuler, and G. V. Shlyapnikov, Nature Physics **6**, 900 (2010).
 - [12] I. Tikhonenkov, A. Vardi, J. Anglin, and D. Cohen, Phys. Rev. Lett. **110**, 050401 (2013).
 - [13] O. Dutta, M. Gajda, P. Hauke, M. Lewenstein, D. S. Lühman, B. A. Malomed, T. Sowinski, and J. Zakrzewski, Rep. Prog. Phys. **78**, 066001 (2015).
 - [14] A. Dey and A. Vardi, Phys. Rev. A **95**, 033630 (2017).
 - [15] T. Lahaye, C. Menotti, C. L. Santos, M. Lewenstein, and T. Pfau, Rep. Prog. Phys. **72**, 126401 (2009).
 - [16] C. Trefzger, C. Menotti, B. Capogrosso-Sansone, and M. Lewenstein, J. Phys. B **44**, 193001 (2011).
 - [17] V. Oganessian and D. A. Huse, Phys. Rev. B **75**, 155111 (2007).
 - [18] Y. Y. Atas, E. Bogomolny, O. Giraud, and G. Roux, Phys. Rev. Lett. **110**, 084101 (2013).
 - [19] N. D. Chavda, H. N. Deota, and V. K. B. Kota, Phys. Lett. A **378**, 3012 (2014).

Appendix A: The eigenstates of a single trimer

The Hamiltonian of a single-particle linear trimer ($N_\alpha = 1$ and $u = 0$) is diagonal in the basis

$$\begin{aligned}
 |\text{sym}\rangle &= \frac{1}{2}(|1\rangle + \sqrt{2}|2\rangle + |3\rangle), \\
 |\text{anti}\rangle &= \frac{1}{2}(|1\rangle - \sqrt{2}|2\rangle + |3\rangle), \\
 |\text{dark}\rangle &= \frac{1}{\sqrt{2}}(|1\rangle - |3\rangle).
 \end{aligned} \tag{A1}$$

with the corresponding energies

$$\omega_{\text{sym}} = -\omega_0, \quad \omega_{\text{anti}} = +\omega_0, \quad \omega_{\text{dark}} = 0, \tag{A2}$$

where $\omega_0 = K/\sqrt{2}$. The many-body Hamiltonian can be rewritten as

$$H_{\text{trimer}} = \omega_0(\hat{n}_{\text{anti}} - \hat{n}_{\text{sym}}) \tag{A3}$$

where the occupation operators are associated with

$$\begin{aligned}
 \hat{a}_{\text{sym}} &= \frac{1}{2}(\hat{a}_1 + \sqrt{2}\hat{a}_2 + \hat{a}_3), \\
 \hat{a}_{\text{anti}} &= \frac{1}{2}(\hat{a}_1 - \sqrt{2}\hat{a}_2 + \hat{a}_3), \\
 \hat{a}_{\text{dark}} &= \frac{1}{\sqrt{2}}(\hat{a}_1 - \hat{a}_3).
 \end{aligned} \tag{A4}$$

The third occupation operator is \hat{n}_{dark} , whose scaled version (in the classical context) or scaled expectation value (in the quantum context) is denoted as I_{dark} .

If the spectrum of the Hamiltonian in Eq. (A3) was presented in the diagram of Fig. 1a, it would form a triangular lattice of points that represent all possible occupations, with corners at $(-\omega_0, 0)$, $(0, 1)$, and $(\omega_0, 0)$. These corners correspond to coherent states, meaning that all particles occupy a single orbital. More generally, one can characterize each eigenstate by its one-particle purity. For this purpose, one defines the one-particle probability matrix

$$\rho_{jk}^{(1)} = \frac{1}{N} \langle \hat{a}_j^\dagger \hat{a}_k \rangle. \tag{A5}$$

The purity is then evaluated as

$$\text{purity} = \text{trace} \left\{ [\rho^{(1)}]^2 \right\} \in [1/3, 1]. \tag{A6}$$

The inverse purity tells us what is the number of orbitals that “participate” in the formation of the many-body state (only one for coherent states). Once the interaction is turned on, as in Fig. 1a, the central eigenstates of the spectrum mix to form incoherent (down to minimum purity $\approx 1/3$) eigenstates that dwell in the chaotic sea.

Considering the interacting trimer, at the low energy range we have remnants of (almost) unperturbed eigenstates (purity ≈ 1). In the upper energy range one should distinguish between two borders. The first one is the edge of the chaotic sea, whose determination is discussed in Appendix B; up to this energy the eigenstates are like random waves that dwell on the energy surface. The second is the threshold for self-trapping: above this value the energy surface is composed of 3 disjoint regions around $I_j \sim 1$ with $j = 1, 2, 3$. Classical clouds cannot migrate between these regions. Quantum mechanically, we see the formation of states that occupy the middle site, or cat superposition states that are self-trapped in either the left or the right sites; the cat states have purity equal to 1/2. The occupation probability density for representative energies is presented in Fig. 7.

Appendix B: Chaotic range determination

Chaotic classical motion can be identified by directly observing the dynamics of individual trajectories on various energy surfaces, for example, via plotting Poincaré

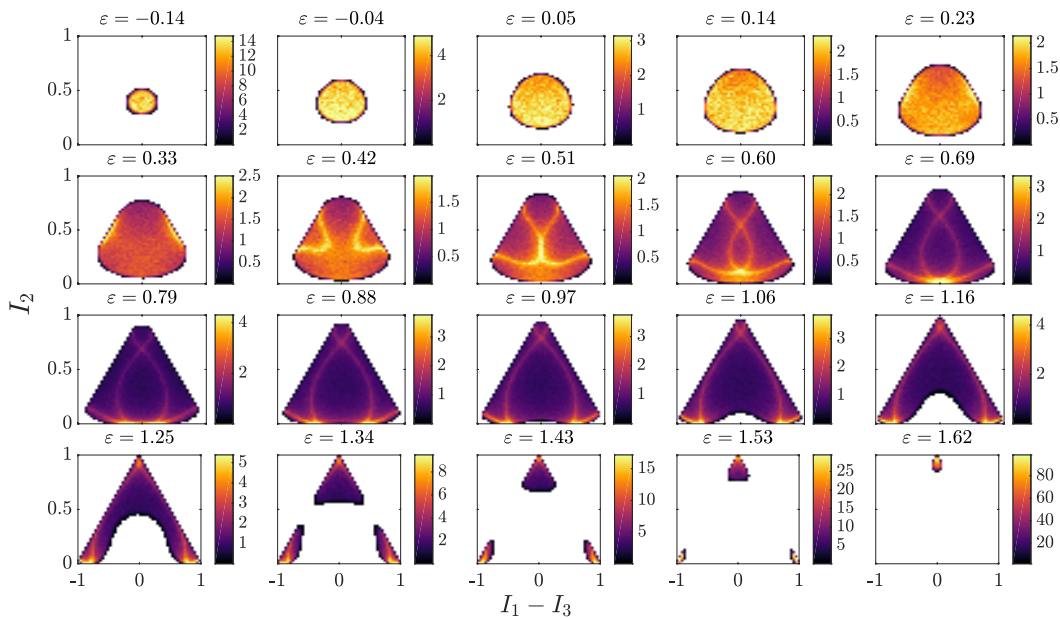


FIG. 7. (Color online) The trimer probability density for representative energy surfaces. The interaction parameter is $u = 3$. The entire spectrum lies within the range $(-0.18, 1.66)$. Self-trapping is observed above $\varepsilon = 1.31$.

sections. Another possibility is to inspect the power spectrum for a variable of interest: a defining property of a chaotic motion is that the Fourier transform of a fluctuating variable exhibits a continuous frequency spectrum. By contrast, the Fourier spectrum of a regular trajectory is made of zero-width delta peaks.

Alternatively, the underlying classical chaos is indicted in the spectral statistics of the many-body system. Let ε_n be an ordered set of energy levels, and $s_n \equiv \varepsilon_{n+1} - \varepsilon_n$ the nearest-neighbor level spacings. It is convenient to inspect the ratios [17–19]

$$r_n = \frac{\min\{s_n, s_{n+1}\}}{\max\{s_n, s_{n+1}\}} \in [0, 1] \quad (\text{B1})$$

Statistical information is obtained from the average $\langle r \rangle$ taken over many levels within a small energy window. Uncorrelated levels yield a Poissonian distribution of spacings, $\langle r \rangle \approx 0.386$, with an underlying quasi-regular classical motion. By contrast, for model Hamiltonians with time-reversal symmetry, level repulsion leads to Wigner distribution with $\langle r \rangle \approx 0.536$, indicating chaotic classical motion.

The function $\langle r \rangle$ evaluated for the trimer Hamiltonian of Eq. (1) is plotted in Fig. 1d. As verified by Poincaré sections, in the central range $0.45 < \varepsilon < 1$ (corresponding to $\langle r \rangle > 0.52$) the classical energy surfaces are almost entirely covered by chaotic trajectories. At other energies the phase space is mixed, with regular islands existing within a chaotic sea. In general, when moving away from the central chaotic region the phase space area occupied by the islands grows, with $\langle r \rangle$ slowly approaching its lower limit. Above $\varepsilon > 1.31$ the trimer nonlinearity

becomes sufficiently strong to cause self-trapping; the reduced dimensionality prevents chaos from appearing, and the motion becomes quasi-integrable. At low energies the system is almost linear and hence again quasi-integrable.

A self-consistent determination of the chaotic range in the spectrum is achieved by locating the energies at which $\langle r \rangle$ crosses the half-way value $(\langle r \rangle_{\text{Poisson}} + \langle r \rangle_{\text{Wigner}})/2 = 0.461$; this happens at $\varepsilon = 0.26$ and $\varepsilon = 1.23$. At these energies the distribution of r values agrees to an equal degree with both limiting distributions; accordingly, there is no sharp change in the nature of the classical motion slightly above or slightly below the border energies.

Limitations of the $\langle r \rangle$ statistic.— Close to the edges of the trimer spectrum, the density of states is very low and meaningful statistics cannot be obtained: the locally-averaged level spacing correlation function, $\langle r \rangle$, becomes strongly dependent on the size of the averaging window and yields nonsensical values. Those bad regions were removed from Fig. 1d.

Additionally, energy levels belonging to distinct symmetry subspaces are not correlated even if the underlying dynamics is chaotic. Therefore, the evaluation of r must always be performed on levels that belong to the same symmetry subspace.

Appendix C: Classical simulations

Constructing a classical cloud.— The initial condition for any classical simulations is a cloud of 1000 phase space points, uniformly distributed over the entire energy surface (E_0, x_0) , or correspondingly, $(\varepsilon_{L,0}, \varepsilon_{R,0})$. Below

we outline the procedure used to generate this distribution.

Let $P = (I_1, I_2, I_3, \varphi_1, \varphi_2, \varphi_3)$ represent a point in the phase space of an isolated trimer, lying on the energy surface ε_0 . First, we generate two sets of N values (where N is some large number), drawn randomly from the uniform distribution $[0, 1]$. Each set is then assigned to one of the two populations $I_{1,2}$; the third population is calculated from $I_3 = 1 - I_1 - I_2$. Similarly, three sets of N values are drawn randomly from the uniform distribution $[0, 2\pi)$, and assigned each to one of the phases $\varphi_{1,2,3}$. Next, we discard all points where $I_3 < 0$ (i.e., $I_1 + I_2 > 1$), since site populations cannot be negative by definition. Afterwards, we calculate the energy ε_P associated with each phase space point P ; all points where $|\varepsilon_0 - \varepsilon_P| > 10^{-4}$ are discarded.

The randomization above is repeated until we collect 1000 points for a trimer with energy $\varepsilon_{L,0}$. Then the same is performed on the second trimer with energy $\varepsilon_{R,0}$, until once again we have 1000 points. The final result is a cloud of 1000 twelve-parameter phase space points $I_{\alpha j}, \varphi_{\alpha j}$ ($\alpha = L, R$ and $j = 1, 2, 3$).

Calculating the power spectrum.— The classical power spectrum, presented in Fig. 1b for $I_{1,3}(t)$ and in Fig. 1c for $I_2(t)$, is an average over 100 independent spectra, each generated from a single long trajectory belonging to the energy surface ε and evolving under Eq. (1). The averaging masks the discrete nature of the spectrum in the regular region, but it allows us to have a representative picture of the frequency support of the entire energy surface.

Calculating the diffusion coefficient.— The diffusion coefficient $D(\varepsilon_L, \varepsilon_R)$ should be representative of the dynamics on the entire energy surface in each of the trimers, implying an average over many initial conditions. The proper procedure consists of generating two power spectra based on two *different* classical trajectories $I_j(t)$, then calculating their overlap integral via Eq. (13), and finally averaging over a large set of resulting D values. In the general case, one may employ Eq. (13) only once, directly using the average spectra as in Fig. 1b,c. However, for $x = 0$ this would result in abnormally high values of D as the two spectra in the overlap integral will always be identical (since $x = 0$ implies $\varepsilon_L = \varepsilon_R$).

Appendix D: The eigenstates of the double trimer

The double-trimer shown in the inset of Fig. 2 remains unchanged under three operations: P_1 , the permutation of sites $\{L1 \leftrightarrow L3, R1 \leftrightarrow R3\}$; P_2 , the permutation of sites $\{L1 \leftrightarrow R1, L2 \leftrightarrow R2, L3 \leftrightarrow R3\}$; and $P_3 = P_1 \cdot P_2$. The Hilbert space of the system contains a total of four symmetry subspaces. The states symmetric/antisymmetric under P_1 are labeled S, A , respectively; similarly, the states sym/anti under P_2 are labeled g, u , respectively. By constructing a new basis from corresponding superpositions of Fock states (i.e., states

that are sym/anti under each of the three operations), the Hamiltonian H assumes a block-diagonal form. For $N/2$ particles in each trimer the dimension of the full Hilbert space is $d_N = [(N/2 + 1)(N/2 + 2)/2]^2$, while each block contains approximately $d_N/4$ states. Thus, by exploiting the symmetries of the system the calculational cost of exact diagonalization is reduced, making it possible to reach higher particle numbers.

Within the picture of two weakly interacting trimers, the most intuitive basis for $H_L + H_R$ is the set of direct products of the single-trimer eigenstates, $|\varepsilon_n\rangle |\varepsilon_m\rangle$. Each of these states can be alternatively labeled by its total energy $E = \varepsilon_n/2 + \varepsilon_m/2$ and its energy imbalance $x = \varepsilon_n - \varepsilon_m$. A generic direct product for $x \neq 0$ is formed by a superposition of two same-energy states, both belonging to either the S or the A subspaces,

$$|E, \pm|x\rangle_\gamma = \frac{1}{\sqrt{2}}(|E\rangle_{g,\gamma} \pm |E\rangle_{u,\gamma}) \quad \gamma = A, S \quad (\text{D1})$$

The special case of $x = 0$ appears only in the S subspace, where

$$|E, 0\rangle_S = |E\rangle_{g,S} \quad (\text{D2})$$

The spectral properties of all four subspaces are similar; therefore, it is possible to limit the analysis to only the A subspaces (i.e., Au and Ag), thereby avoiding the complications induced by the $|E, x = 0\rangle$ states.